MEASUREMENTS OF THE BIDIRECTIONAL REFLECTANCE OF SNOW AT FINE SPECTRAL AND ANGULAR RESOLUTION

Thomas H. Painter[1] and Jeff Dozier[2]

ABSTRACT

This paper presents measurements of the bidirectional reflectance factor (BRF) of snow made at fine spectral and angular resolution with the Automated Spectro-Goniometer (ASG) for a range of solar zenith angles (θ_0 = 40-50°) and snow textures (surface grain size = 80 - 240 μm) on two days. Measurements of the stratigraphy of snow texture and density accompanied each day's suite of measurements. The BRF for fine grain, faceted snow exhibited a local backscattering peak at the view zenith near the solar zenith angle, whereas those for medium grain, clustered snow did not have a local backscattering peak. The BRF decreased at all wavelengths for an increase in measured grain radius from 80 μm to 240 μm. However, the decrease in BRF in the visible wavelengths was strongest at θ_r = 80° in the forward direction and strongest for $\lambda > 1.8$ μm near θ_r = 30° in the backward direction. As solar zenith angle decreased from 47° to 41° the BRF increased near nadir for $\lambda \leq 1.03$ μm but decreased with coherent angular structure for $\lambda > 1.03$ μm.

INTRODUCTION

Improvement of quantitative retrievals of snow physical properties from remote sensing will require knowledge of the spectral and angular structure of snow's bidirectional reflectance distribution function. Models for subpixel snow covered area, grain size, albedo, and liquid water content invert directional reflectance data from multi-spectral and hyperspectral remote sensing platforms and field measurements [*Davis et al.*, 1993; *Green et al.*, 2002; *Jin and Simpson*, 2001; *Nolin and Dozier*, 2000; *Painter et al.*, 1998]. A comprehensive knowledge of the bidirectional reflectance of snow allows us to evaluate the range of validity for those models that do not incorporate directional reflectance information or topographic correction and will improve efforts to incorporate directional reflectance into retrievals.

Several investigators have documented portions of the bidirectional reflectance of snow [*Aoki et al.*, 2000; *Dozier et al.*, 1988; *Kuhn*, 1985; *Leroux et al.*, 1998; *O'Brien*, 1975; *Steffen*, 1987], giving us a coarse understanding of its structure and dependencies. Dozier et al [1988] gave the most comprehensive characterization of the BRDF of snow, but the spectrometer they used was sensitive only for $\lambda < 1.0$ μm. From other work, we know that the BRF of snow is most anisotropic at $\lambda > 1.0$ μm. In this work, we present spectroscopic measurements of the bidirectional reflectance factor of snow at 10° angular resolution in the view zenith and azimuth. These measurements address the sensitivity of the BRF of snow to wavelength, snow texture, and solar zenith angle.

METHODS

Site

We measured snow BRF with the Automated Spectro-Goniometer (ASG) in Sherwin Meadows, immediately south of Mammoth Lakes, California at an elevation of 2450 m. Mammoth Lakes lies on the east side of the Sierra Nevada near Mammoth Mountain Ski Area at latitude 37°37' N and longitude 119°02' W.

Bidirectional Reflectance Factor

The Automated Spectro-Goniometer [*Painter et al.*, 2002] collected data with the 10° protocol during the winter 2001 acquisitions. We present the data in terms of the BRF and the *anisotropy factor* (ANIF) that facilitates

Presented at the 70th Annual Meeting of the Western Snow Conference, 2002
[1]Institute for Computational Earth System Science, University of California, Santa Barbara, California
Now at: CSES/CIRES, University of Colorado, Boulder, Colorado
[2]Donald Bren School of Environmental Science and Management, University of California, Santa Barbara

the analysis of the spectral variability in BRF data [*Sandmeier and Itten*, 1999]. The ANIF is given by normalizing the BRF by the nadir BRF.

$$BRF(\theta_0,\phi_0;\theta_r,\phi_r) = \frac{\pi I(\theta_r,\phi_r)}{\cos\theta_0 E(\theta_0,\phi_0)}$$

$$ANIF(\theta_0,\phi_0;\theta_r,\phi_r) = \frac{BRF(\theta_0,\phi_0;\theta_r,\phi_r)}{BRF(\theta_0,\phi_0;0,0)}$$

where I is the radiance reflected from the surface into reflectance angle and azimuth θ_r, ϕ_r given irradiance E with incident angle and azimuth θ_0, ϕ_0.

Spectral Atmospheric Optical Depth

We used a Reagan Sun Photometer [*Optical Sciences Center*] to characterize the atmospheric optical depth for ASG acquisitions. The sun photometer has a 10-channel parallel co-aligned field-of-view tube with a 3.2° field-of-view. The sun photometer collected voltage measurements once per minute at the following wavelengths: 0.382, 0.41, 0.501, 0.611, 0.669, 0.721, 0.78, 0.872, 0.94, and 1.03 μm with full-width half-maxima of 0.008-0.012 μm. We used the Langley method to calculate spectral atmospheric optical depth [*Stephens*, 1994].

Snowpack Characterization

For each suite of acquisitions, we sampled a snow pit immediately adjacent to the snow target and collected snow samples from the target for characterization of snow grain size and snow grain morphology.

We sampled each snow pit for density and temperature at the end of a day's suite of ASG acquisitions. Density was measured with a 250 ml snow cutter for depths 0-1 and 1-2 cm, a 500 ml snow cutter for depths 2-5, 5-8, and 8-11 cm, and a 1000 ml snow cutter for depths 11-21, 21-31, and 31-41 cm. Snow temperature was measured with a dial stem thermometer.

Snow samples were collected from the target for depths 0-10 cm, 10-20 cm, and 20-30 cm. We then transported these samples to a cold room at the nearby Sierra Nevada Aquatic Research Laboratory. The samples were stored for transit in an electric cooler that had been prepared with snow stored at -10°C and kept insulated in a snow pit near the target site. We analyzed the serial photographs of sample cross-sections in 2 cm intervals for the sphere radius with the surface-area-to-volume ratio determined with the stereological relationships [*Davis et al.*, 1987].

RESULTS

Acquisition Set

The acquisition set from the ASG consists of 1 scan for fine-grain snow on February 23, 2001, and 2 scans for medium-grain snow on March 13, 2001. Herein, we refer to the February 23 acquisition as F1 and the two March 13 acquisitions as M1 and M2. The respective solar ephemerides for these acquisitions are shown in Table 1.

Table 1. Solar ephemeris data for ASG acquisitions.

	February 23, 2001 F1	**March 13, 2001** M1, M2
θ_0, ϕ_0	47.3°, 176.9°	46.5°, 144.3°
θ_0, ϕ_0		41.9°, 161.0°

Snowpack Characterization

Figure 1 shows the density and temperature profiles for the snow pits sampled on February 23 and March 13. Figure 2 shows the grain size profiles as determined with stereological analysis of the snow samples. Snow grain shapes on February 23 consisted primarily of slightly rounded remnants of the original plates and dendritic forms (Figure 3), whereas on March 13, surface grains were primarily grain clusters formed through melt-freeze cycling. On both dates, the snow temperature was less than 0°C at the time of acquisition.

(a)

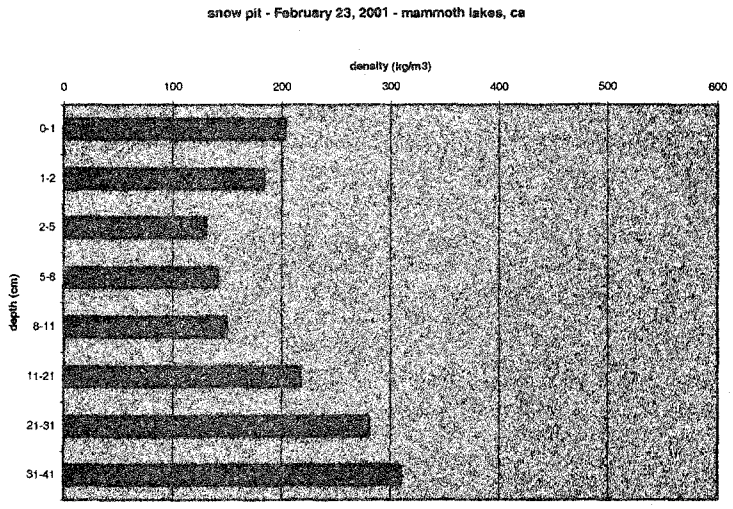

(b)

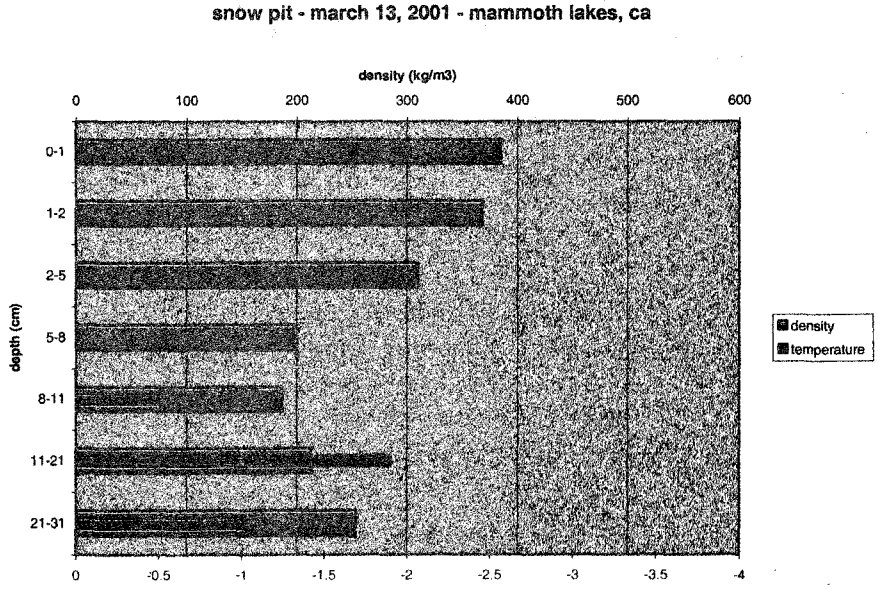

Figure 1 Snow density and temperature stratigraphy for (a) February 23 and (b) March 13 ASG acquisitions (instrument failure prevented measuring temperature on February 23).

On February 23, density decreased from 200 kg/m^3 near the surface to 130-150 kg/m^3 at 2-11 cm depth and increased to greater than 300 kg/m^3 between 31 and 41 cm depth (Figure 1). This pack had increased in density over 2 days since a large snowfall with density ~80-100 kg/m^3. On March 13, density decreased from 380 kg/m^3 in the top 2 cm to 180 kg/m^3 between 8 and 11 cm and then increased to ~ 250 kg/m^3 in the 21-31 cm layer. Liquid water from surface melting in the top 2 cm had increased the density by forming grain clusters and accelerating settling. March 13 came a few days into a period of above normal air temperatures and clear skies that lasted through the remainder of March. Therefore, surface layers exhibited greater densification while the deeper layers had not yet densified appreciably.

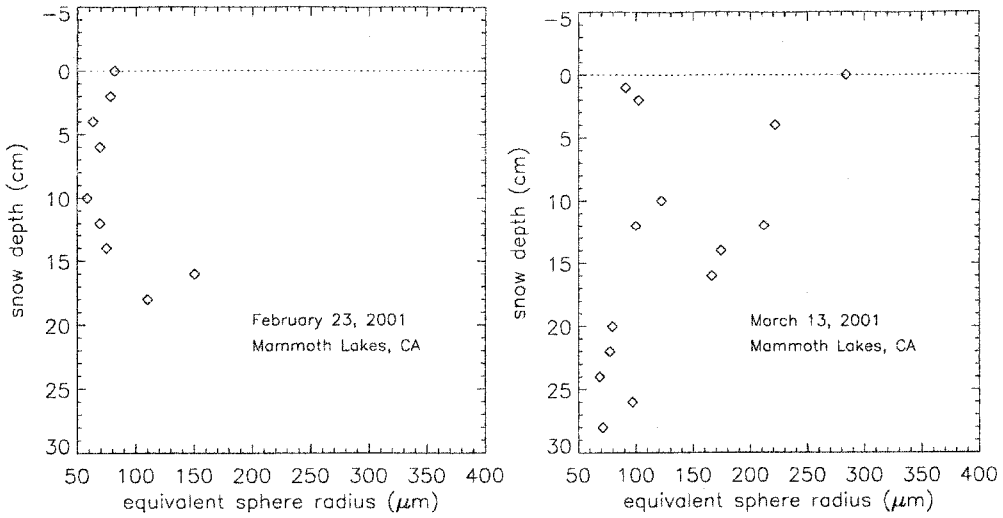

Figure 2 Grain size stratigraphy for ASG target snowpack as determined by stereological analysis.

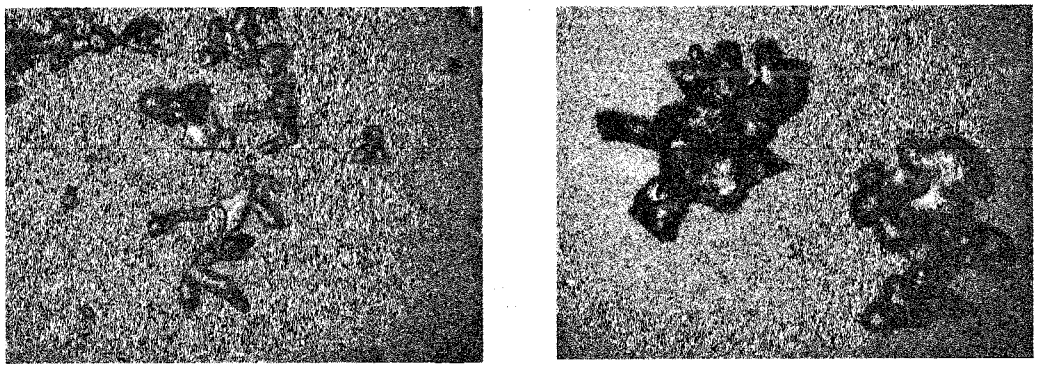

Figure 3 Photomicroscope images of snow morphology for February 23, 2001 (left) and March 13, 2001 (right).

The stratigraphy of grain size exhibited a similar time series (Figure 2). Grain size on February 23 was relatively constant with depth, increasing slightly from ~70 μm at depths 0–16 cm to ~125 μm at 18-20 cm. The entire snowpack (52 cm) came from consecutive storms separated by cold temperatures and slow grain growth. Grain size on March 13 showed greater scatter and values up to 284 μm in the top 5 cm. Grain size ranged from 100 to 210 μm between depths of 10 and 18 cm, and grain size decreased to a range of 65 to 95 μm between depths of 20 and 30 cm. The grain size stratigraphy on March 13 exhibits the same response to warm temperatures and full insolation as that by the stratigraphy of density.

Atmospheric Optical Depth

The sun photometer was not available for the February 23 acquisition. Figure 4 shows the Langley derived spectral optical depths for the March 13, 2001 acquisitions. The stability of instantaneous total optical depths (not shown) during the March 13 acquisitions showed that atmospheric conditions remained constant.

BRF Relative to View Azimuth

Figure 5Figure 6Figure 7 show the BRF spectra and ANIF spectra for all view zenith angles for view azimuths 0°, 90°, and 180° for the F1, M1, and M2 ASG acquisitions, respectively. Bad data existed at (θ_r = 40°,70°; ϕ_r = 0°), at the *occultation geometry* in the F1 data, and at the occultation geometry in the M2 data. All BRF spectra exhibit noise near λ = 1.85 μm and 2.5 μm that comes from the low signal to noise in these water vapor absorption features.

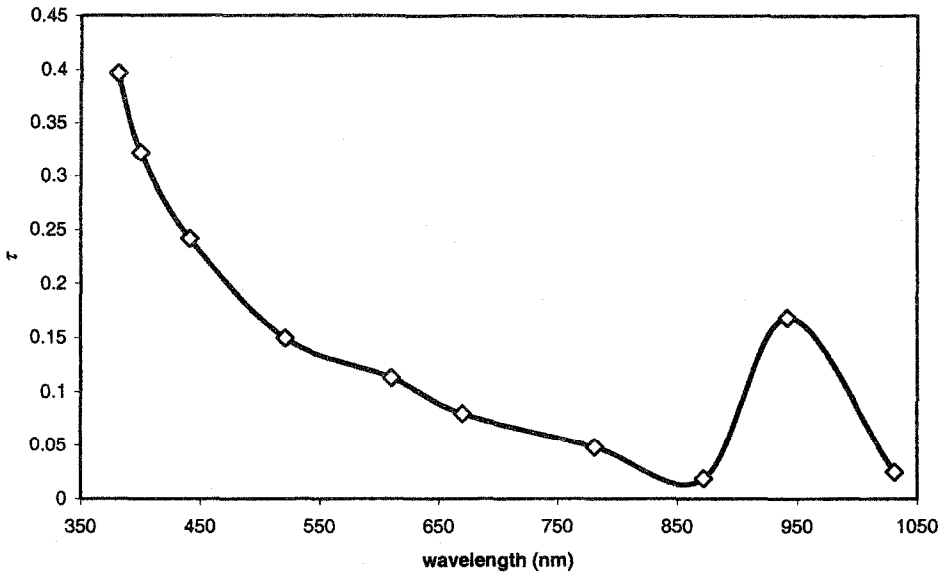

Figure 4. Optical depth spectrum from Langley calculations for the March 13, 2001 measurements at Sherwin Meadows, CA

The F1 BRF spectra show a small local backscattering reflectance peak at $\theta_r \cong 40°$ for $\lambda > 0.9$ μm (Figure 5). The M1 and M2 BRF spectra do not show this peak. Steffen [1987] observed this backscattering peak near the solar zenith in the shorter wavelength band 0.5 μm $\leq \lambda \leq$ 0.6 μm. While it has similar bidirectional structure as the retro-solar reflectance peak for vegetation (the 'hot spot'), the mechanism is different. The vegetation hot spot is due to the absence of shadowed surface in the field-of-view whereas for snow, the retro-solar peak, if present, is primarily due to local peaks in the single-scattering phase function (Appendix I) associated with greater faceting on the snow grains.

The F1 data show high reflectance that is consistent with the fine grain size (Figure 5). The nadir BRF was 0.98 at λ = 0.55 μm, 0.75 at λ = 1.03 μm, 0.55 at λ = 1.3 μm, and 0.2 at λ = 2.25 μm. In the forward half of the solar principal plane ($\phi_r = 0°$), BRF exhibited the largest zenithal increase. Anisotropic factors ranged from 1.5 at λ = 0.55 μm to 4.0 at λ = 2.25. The BRF in the perpendicular plane ($\phi_r = 90°$) exhibited a small, monotonic zenithal decrease at wavelengths $\lambda \leq 0.98$ μm and a small monotonic zenithal increase that increased with wavelength at wavelengths $\lambda \geq 0.98$ μm. In the backscattering half of the solar principal plane ($\phi_r = 180°$), the BRF exhibited a larger monotonic zenithal decrease at $\lambda \leq 0.98\mu$m and little change at other wavelengths. However, the slight backscattering peak at $\theta_r = 40°$ occurred at all wavelengths > 0.8 μm, increasing in ANIF with increasing wavelength.

M1 and M2 show lower reflectance than that for F1, consistent with the measured increase in grain size (Figure 6Figure 7). In the M1 acquisition ($\theta_0 = 47°$), the nadir BRF was 0.99 at λ = 0.55 μm, 0.5 at λ = 1.03 μm, 0.25 at λ = 1.3 μm, and 0.07 at λ = 2.25 μm (Figure 6). The BRF for $\phi_r = 0°$ increased monotonically at all wavelengths to lower reflectance than in the F1 data but with larger ANIF. BRF in the perpendicular plane decreased slightly for $\lambda \leq 0.86$ μm and increased for $\lambda \geq 0.86$ μm with larger ANIF in the perpendicular plane than exhibited in the F1 data. For $\phi_r = 180°$, the BRF decreased with zenith angle for $\lambda \leq 0.97$ μm and increased with zenith angle at longer wavelengths. The magnitude of ANIF change indicates that the M1 data had a greater relative change with view zenith than the F1 data. As with the F1 data, the M1 data exhibited a backscattering peak at θ_r = 50°.

The M1 and M2 data ($\theta_0 = 41°$) had only subtle differences (Figure 7), as one would expect given that the difference in solar zenith angle between the two was 6°. M2 had a smaller increase in BRF with increasing view zenith across the spectrum for $\phi_r = 0°$. In the perpendicular plane, M2 had a larger zenithal decrease for $\lambda \leq 0.95$ μm and a smaller zenithal increase for $\lambda \geq 0.95$ μm. For $\phi_r = 180°$, M2 had a larger zenithal decrease for $\lambda \leq 1.17$

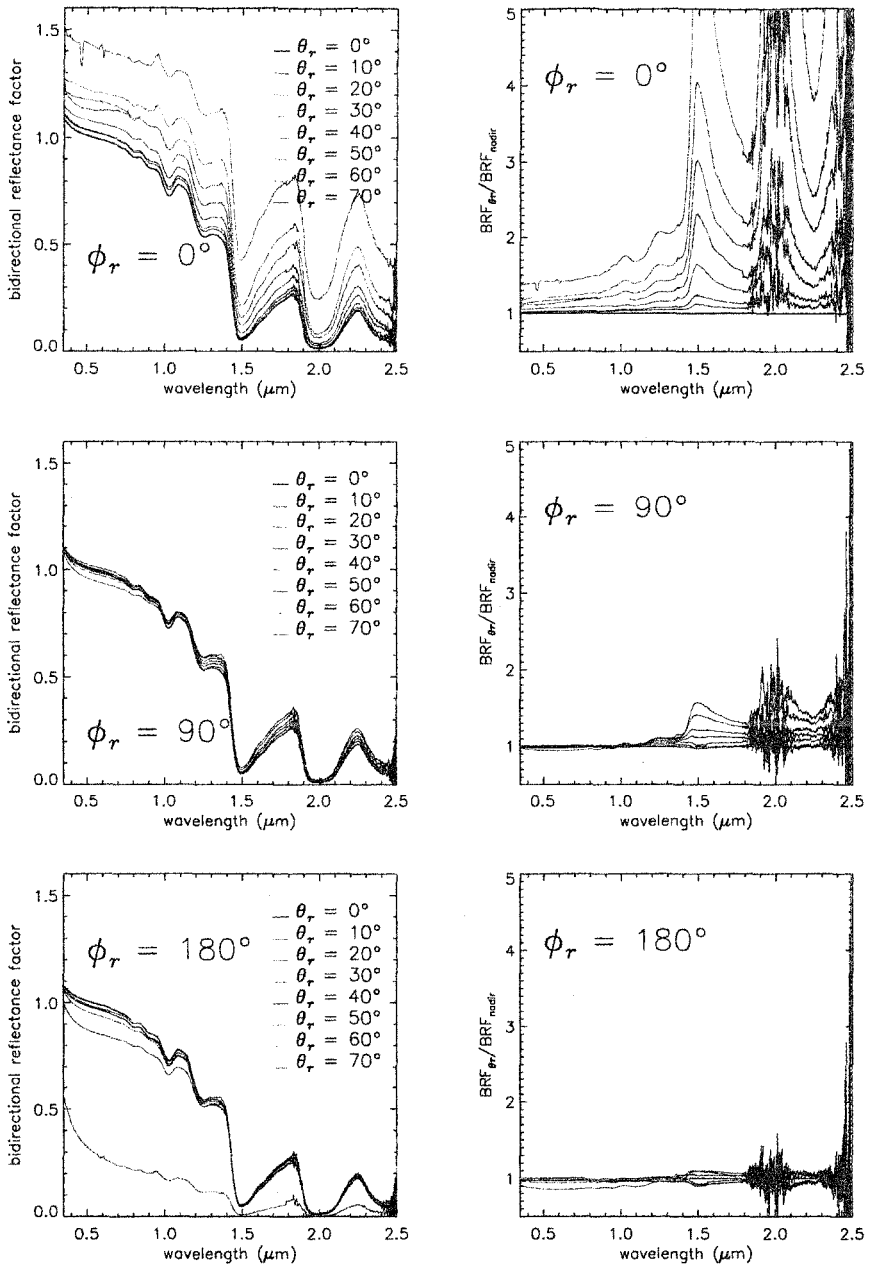

Figure 5. BRF spectra (left) and the ANIF (right) from the F1 ASG acquisition ($\theta_0 = 47°$, surface grain size = 80 μm) for all view zenith angles at view azimuth angles 0°, 90°, and 180°. The spectrum for $\theta_r = 50°$, $\phi_r = 180°$ is much lower due to occlusion of the sun by the ASG foreoptic.

μm and remained nearly unchanged for $\lambda \geq 1.17$ μm. The outlier spectrum in the backscattering half of the principal plane at $\theta_r = 40°$ was an artifact of occultation of the sun by the goniometer.

Angular Structure of the BRF Relative to Wavelength

Figure 8Figure 9Figure 10 show the polar plots of the BRF for six wavelengths across the spectrum for the respective ASG acquisitions. These figures show the angular structure of the bidirectional reflectance factor.

In all acquisitions, the BRF structure drifted from convex about the forward half of the solar principal plane ($\phi_r = 0°$) at shorter wavelengths to concave with respect to the forward direction. The concave structure develops because at longer wavelengths, the single-scattering co-albedo (absorption) is greater and single scattering dominates the intensity of reflected radiation. The angular structure of the BRF at longer wavelengths where single scattering dominates should mimic the mapping of the phase function, at an oblique incidence, into the view

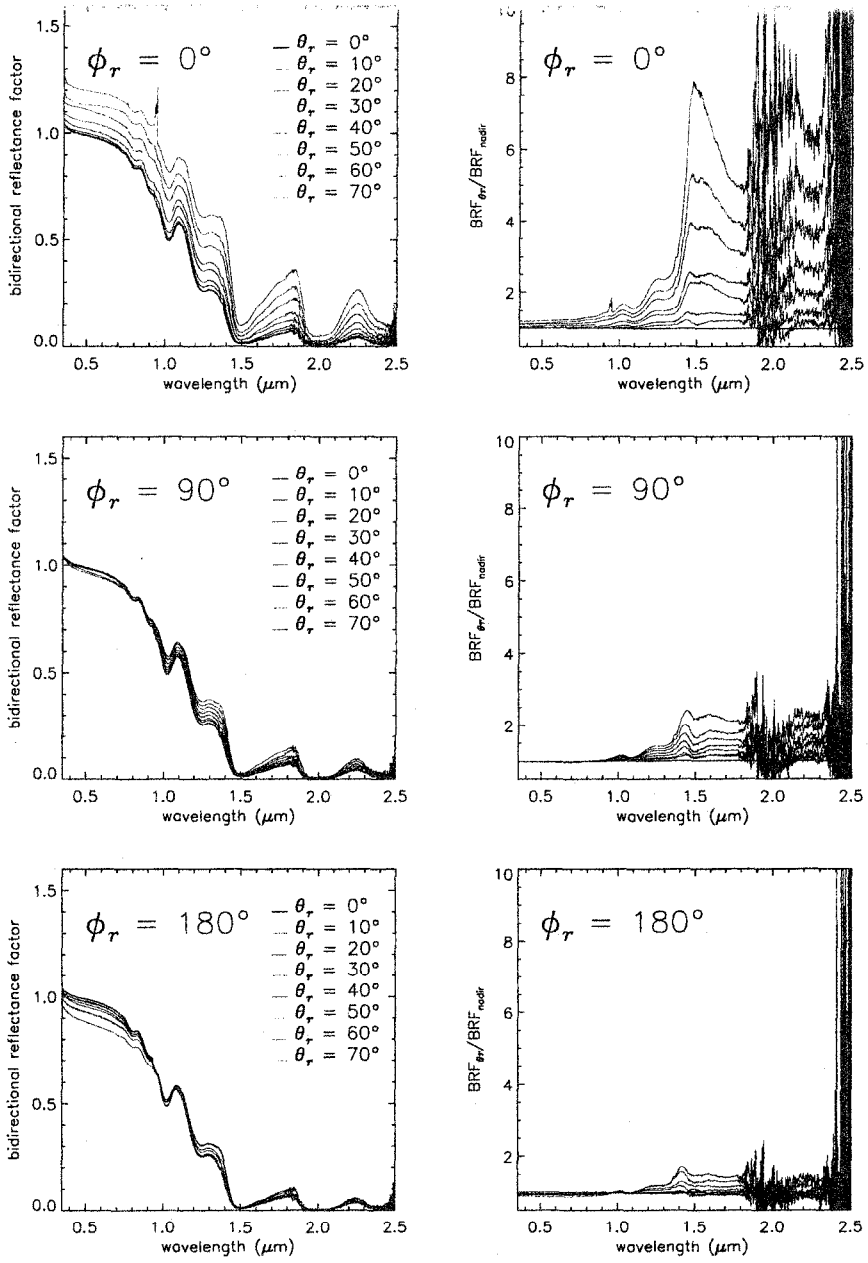

Figure 6. BRF spectra (left) and the ANIF (right) from the M1 ASG acquisition (θ_0 = 47°, surface grain size = 284 μm).

hemisphere. This produced the concave angular structure. Warren [1982] describes the intersection of the scattering phase function with the surface in detail.

The magnitudes of BRF for the M1 and M2 acquisitions were lower than those for the F1 acquisition, consistent with the larger grain sizes on March 13. The M1 data (θ_0= 47°) exhibited higher BRF values and greater forward reflectance anisotropy than the M2 data (θ_0 = 41°), consistent with the larger solar zenith angle.

The structure of the F1 data remained slightly convex at wavelengths up through 1.03 μm whereas the structure of the M1 and M2 data became concave at 1.03 μm.

CONCLUSIONS

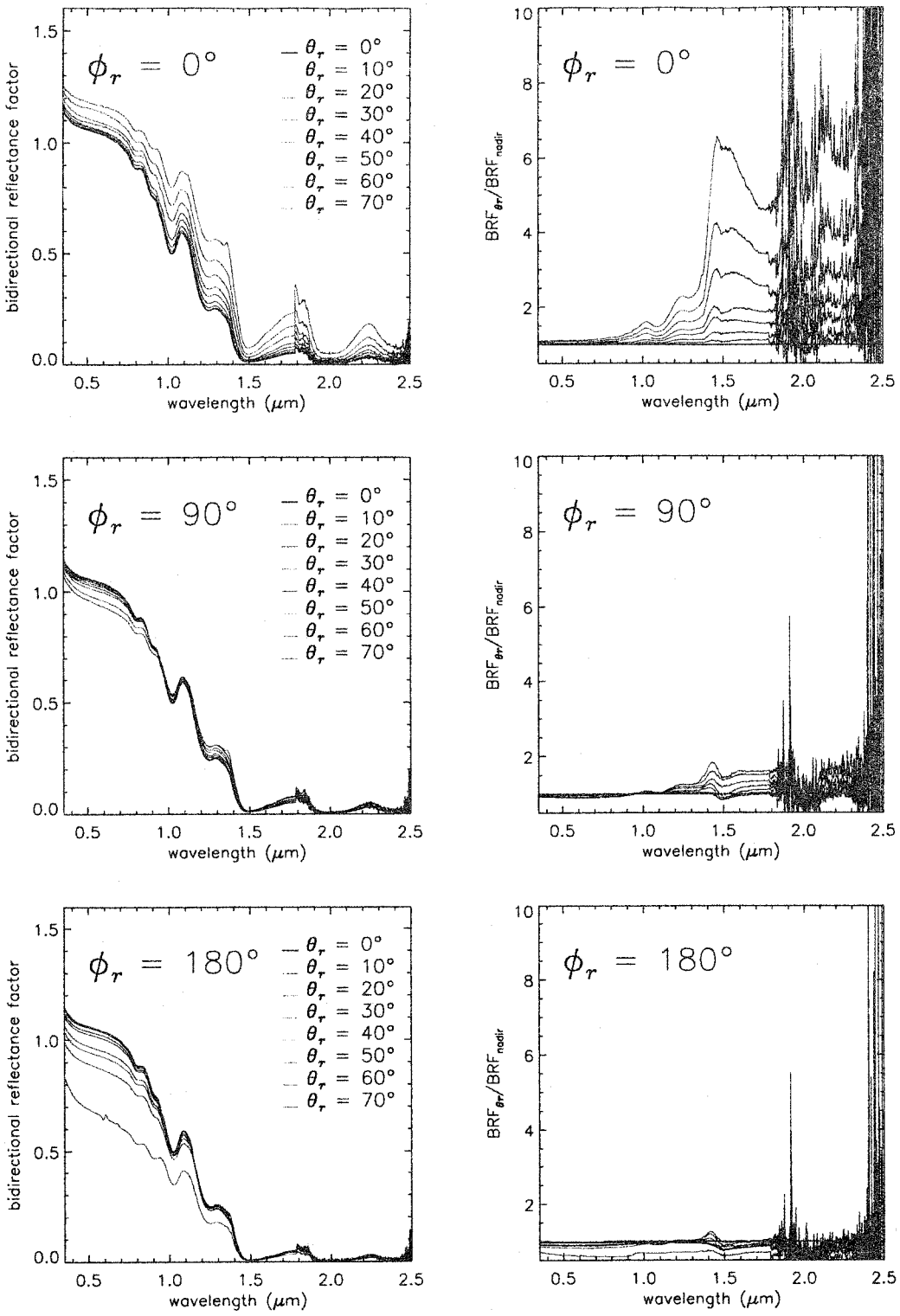

Figure 7. BRF spectra (left) and the ANIF (right) from the M2 ASG acquisition (θ_0 = 41°, surface grain size = 284 μm).

This paper presented measurements at high spectral and angular resolution of the bidirectional reflectance factor of snow. Measurements were made on two dates for fine grain and medium grain snow at solar zeniths 41°-47°. The BRF spectra for fine grain snow had a small backscattering peak at θ_r = 50°, whereas the BRF distributions for medium grain snow did not. The fine grain snow had remnants of the original dendritic morphology that can have a single-scattering phase function with a strong backscattering peak. The backscattering

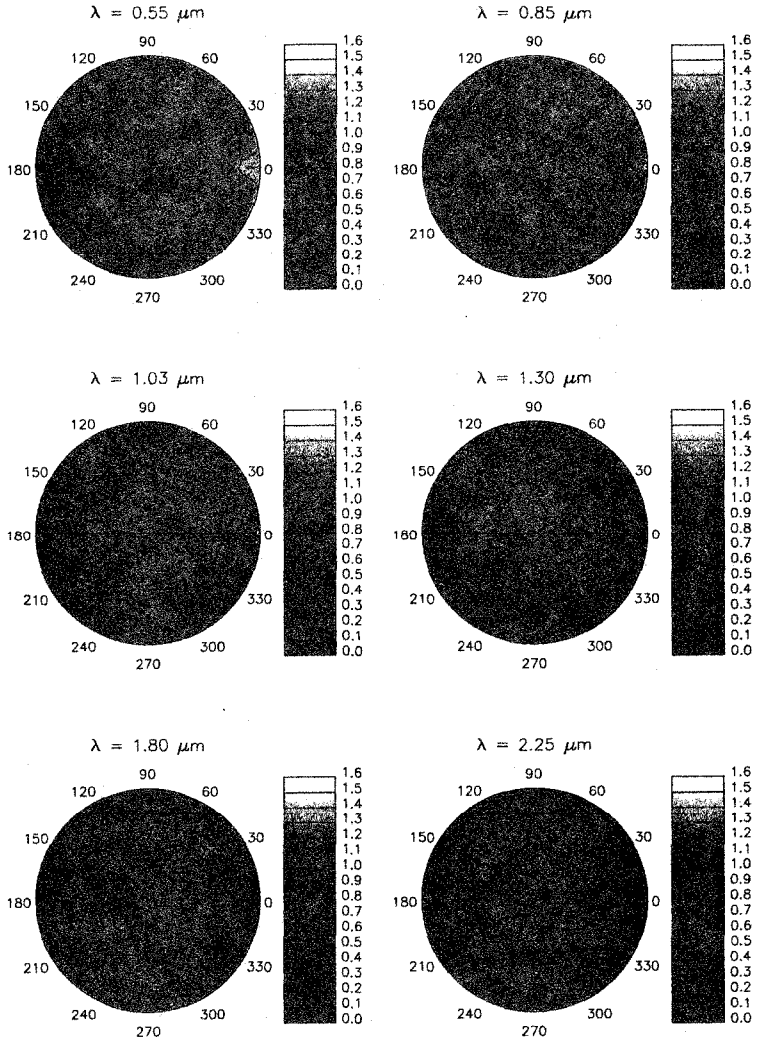

Figure 8. Polar plots of the BRF for all view angles for the February 23 ASG acquisition for 6 wavelengths across the spectrum. The radial distance from the center of each plot represents the view zenith angle. Rotation about the center represents a change in azimuth. The azimuth angle of 0° is the forward reflectance half of the solar principal plane.

peak in the phase function then produces a retro-solar reflectance peak. The medium grain snow consisted mostly of grain clusters that most likely lack the backscattering peak in the phase function.

Further work will investigate the BRF under a larger range of solar zenith angles and for a larger range of particle sizes and morphologies. A thorough investigation of the relationship between the variables retrieved with stereological analysis (surface density, volume density, etc.) and the true particle shape, size, and size distribution is also needed.

REFERENCES

Aoki, T., M. Fukabori, A. Hachikubo, Y. Tachibana, and F. Nishio, Effects of snow physical parameters on spectral albedo and bidirectional reflectance of snow surface, *Journal of Geophysical Research–Atmospheres, 105* (D8), 10219-10236, 2000.

Davis, R.E., J. Dozier, and R. Perla, Measurement of snow grain properties, in *Seasonal Snowcover: Physics, Chemistry, Hydrology*, edited by W.J. Orville-Thomas, and H.G. Jones, pp. 53-74, D. Reidel, Dordrecht, 1987.

Davis, R.E., A.W. Nolin, R. Jordan, and J. Dozier, Towards predicting temporal changes of the spectral signature of snow in visible and near-infrared wavelengths, *Annals of Glaciology, 17*, 143-148, 1993.

Dozier, J., R.E. Davis, A.T.C. Chang, and K. Brown, The spectral bidirectional reflectance of snow, in *4th International Colloquium on Spectral Signatures of Objects in Remote Sensing*, pp. 87-92, Aussois, France, 1988.

Green, R.O., J. Dozier, D.A. Roberts, and T.H. Painter, Spectral snow reflectance models for grain size and liquid water fraction in melting snow for the solar reflected spectrum, *Annals of Glaciology, (in press)*, 2002.

Jin, Z.H., and J.J. Simpson, Anisotropic reflectance of snow observed from space over the Arctic and its effect on solar energy balance, *Remote Sensing of Environment, 75* (1), 63-75, 2001.

Kuhn, M., Bidirectional reflectance of polar and alpine snow surfaces, *Annals of Glaciology, 6*, 164-167, 1985.

Leroux, C., J.L. Deuze, P. Goloub, C. Sergent, and M. Fily, Ground measurements of the polarized bidirectional reflectance of snow in the near-infrared spectral domain: Comparisons with model results, *Journal of Geophysical Research–Atmospheres, 103* (D16), 19721-19731, 1998.

Nolin, A.W., and J. Dozier, A hyperspectral method for remotely sensing the grain size of snow, *Remote Sensing of Environment, 74* (2), 207-216, 2000.

O'Brien, H., Munis, R. H., Red and near-infrared spectral reflectance of snow, CRREL, 1975.

Optical Sciences Center, University of Arizona, 2001.

Painter, T.H., B.A. Paden, and J. Dozier, Automated Spectro-Goniometer: a spherical robot goniometer for the measurement of the bidirectional reflectance of snow, *IEEE Transactions on Robotics and Automation, in review*, 2002.

Painter, T.H., D.A. Roberts, R.O. Green, and J. Dozier, The effect of grain size on spectral mixture analysis of snow-covered area from AVIRIS data, *Remote Sensing of Environment, 65* (3), 320-332, 1998.

Sandmeier, S.R., and K.I. Itten, A field goniometer system (FIGOS) for acquisition of hyperspectral BRDF data, *IEEE Transactions on Geoscience and Remote Sensing, 37* (2 PT2), 978-986, 1999.

Steffen, K., Bidirectional reflectance of snow at 500-600 nm, in *Large Scale Effects of Seasonal Snow Sover*, edited by B. Goodison, R.G. Barry, and J. Dozier, pp. 415-425, IAHS Publication 166, Wallingford, UK, 1987.

Stephens, G.L., *Remote Sensing of the Lower Atmosphere*, 523 pp., Oxford University Press, Oxford, 1994.

Warren, S.G., Optical properties of snow, *Reviews of Geophysics and Space Physics, 20* (1), 67-89, 1982.

ACKNOWLEDGMENTS

This research was funded by the NASA Interdisciplinary Science Project "Hydrology, Hydrochemistry, and Remote Sensing in Seasonally Snow-Covered Alpine Drainage Basins". We thank Dan Dawson and Scott Roripaugh of the Sierra Nevada Aquatic Research Laboratory (SNARL) for their assistance. We thank Robert E. Davis of the U.S. Army Corps of Engineers Cold Regions Research and Engineering Laboratory for the use of the snow microtome and Ian McCubbin and Robert O. Green of the Jet Propulsion Laboratory AVIRIS team for the use and assistance with the sun photometer.

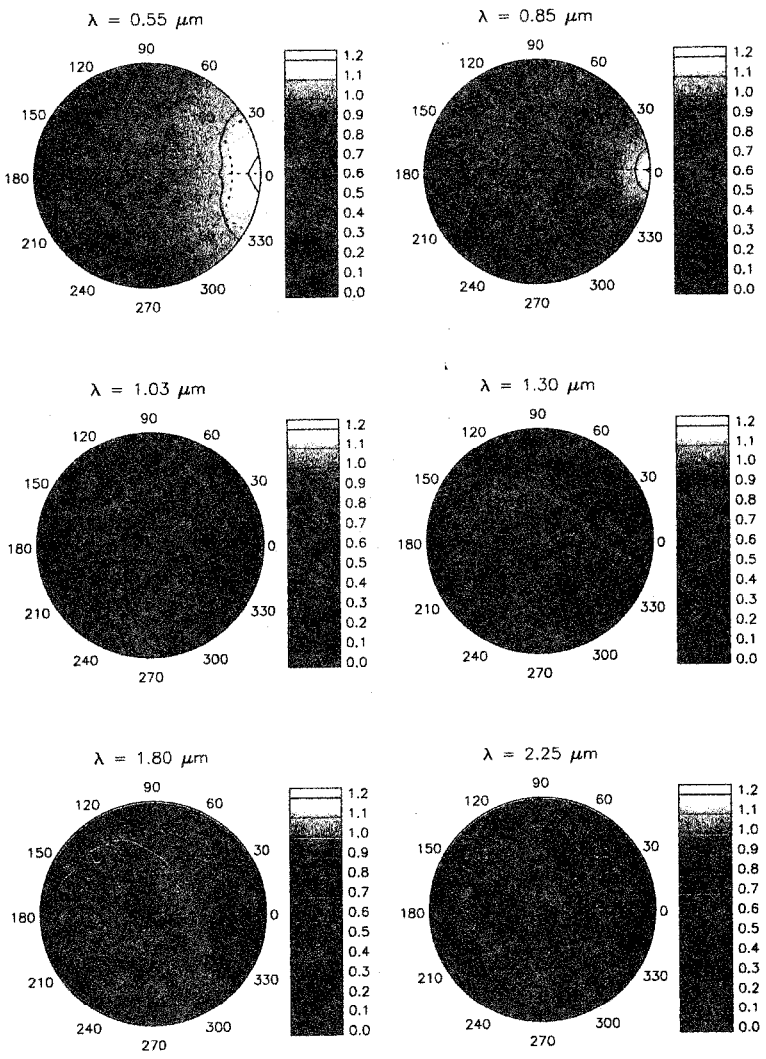

Figure 9. Polar plots of the BRF for all view angles for the first March 13 ASG acquisition ($\theta_0 = 47°$).

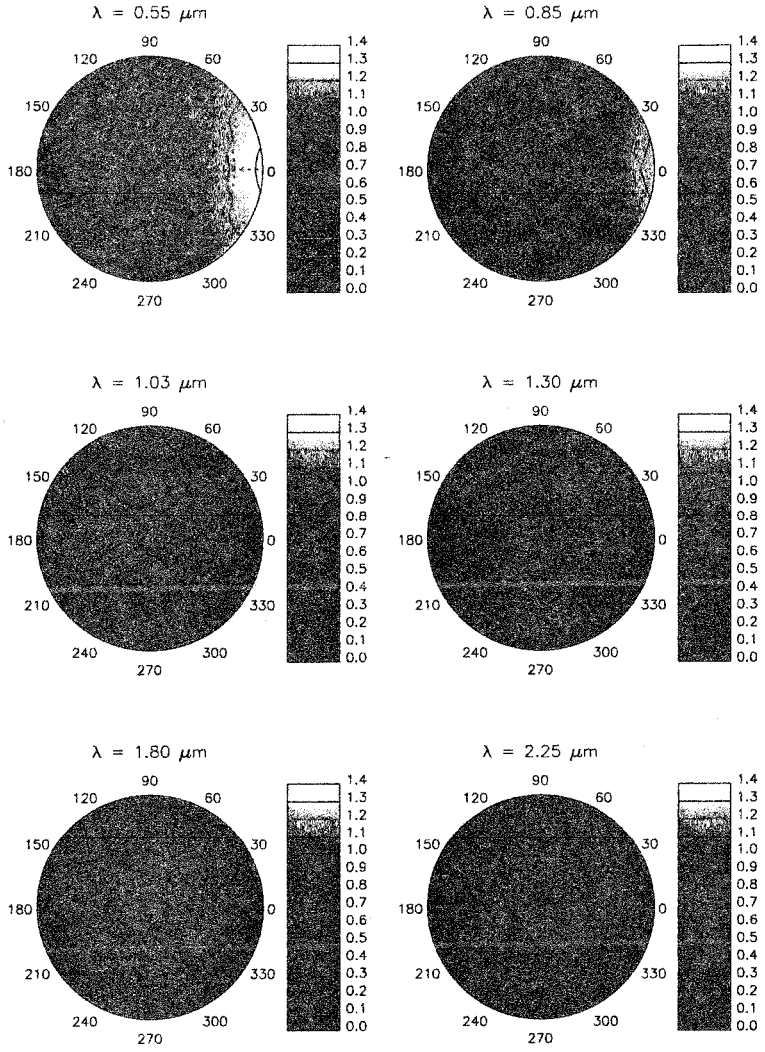

Figure 10. Polar plots of the BRF for the second March 13 ASG acquisition (acquisition ($\theta_0 = 41°$).